ADVANCED FUNCTIONAL MATERIALS
www.afm-journal.de

# All-in-One: An Interwoven Dual-Phase Strategy for Acousto-Mechanical Multifunctionality in Microlattice Metamaterials

*Zhendong Li, Kexin Zeng, Zichao Guo, Zhonggang Wang,* Xiang Yu, Xinwei Li,* and Li Cheng**

**Multifunctional materials that integrate noise absorption, high stiffness, and isotropic elasticity are increasingly sought after for all-in-one applications. However, conventional microlattice metamaterials—whether truss, shell, or plate—often excel in only one property and struggle to embrace all due to structural constraints. Herein, this work presents a new additive concept—via interweaving different lattice architectures to simultaneously enhance both sound absorption and elastic properties in microlattices. The interwoven design strategy starts by analyzing a particular structure, introducing a reinforcing structure to partition air domains, compensate for local stiffness deficiencies, and improve structural integrity. As a proof of concept, the focus is on using an octet truss as the original phase and a customized truss as the reinforcing phase. The methodology enables highly customizable geometric configurations, harnessing machine learning and multi-objective optimization to achieve superior multifunctional performance. Experimental results show that these optimized microlattices overcome traditional physical limitations, simultaneously achieve broadband sound absorption, high stiffness, and elastic isotropy. The broadband absorption results from a finely tuned over-damped resonant response, while the remarkable elastic performance is attributed to efficient load transfer and complementary configurations. This work unveils a groundbreaking design paradigm for innovative multifunctional materials.**

## 1. Introduction

In modern engineering, the pursuit of multifunctional materials has reached new heights. As industries such as construction, aerospace, rail transportation, and military facilities face complex operational challenges, the need for materials that can address these demands is more pressing than ever. Among these challenges, noise pollution stands out as a significant threat, presenting considerable health risks to individuals and communities.[1] Noise pollution is not just an annoyance; it poses a serious threat to human well-being and environmental health. Studies show that prolonged exposure to excessive noise is linked to various health issues, including heart disease and hypertension.[2] Simultaneously, the operational environments of these applications impose rigorous mechanical demands.[3] Materials must mitigate noise and withstand complex external loads, from ultrahigh to unpredictable multidirectional forces.[4] This requirement underscores the urgent need for innovative engineering solutions that seamlessly integrate noise reduction with robust load-bearing capabilities, ensuring safety and comfort in diverse settings—from urban infrastructures to transportation systems. As illustrated in **Figure 1a**, the materials and structures employed must effectively dissipate incident sound energy, thereby reducing noise intensity while resisting elevated loads to prevent yielding under stress. Traditionally, mechanical and acoustic metamaterials have been engineered to excel in specific functions,[5] often surpassing conventional materials in their respective domains. Yet, they fall short of

Z. Li, X. Yu, L. Cheng
Department of Mechanical Engineering
The Hong Kong Polytechnic University
Hong Kong 999077, China
E-mail: li.cheng@polyu.edu.hk

K. Zeng, Z. Guo, Z. Wang
School of Traffic & Transportation Engineering
Central South University
Changsha, Hunan 410075, China
E-mail: wangzg@csu.edu.cn

K. Zeng
Department of Mechanical Engineering
National University of Singapore
Singapore 117575, Singapore

X. Li
Faculty of Science, Agriculture & Engineering
Newcastle University
Singapore 567739, Singapore
E-mail: xinwei.li@ncl.ac.uk

The ORCID identification number(s) for the author(s) of this article can be found under https://doi.org/10.1002/adfm.202420207

**DOI: 10.1002/adfm.202420207**

 

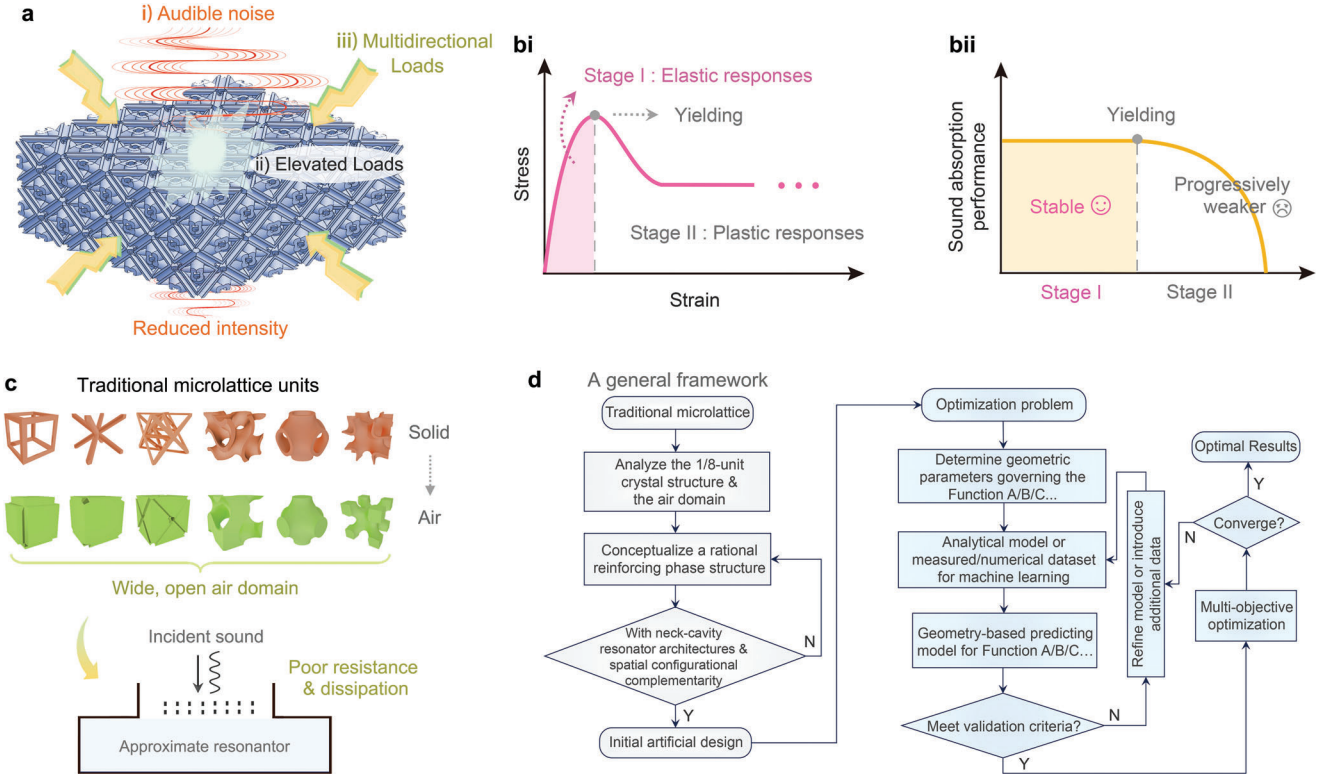


**Figure 1.** Integration of functionality demands, inherent limitations, and proposed solutions. a) Schematic representation of the urgent multifunctional requirements, including noise reduction, capacity to support elevated loads, and ability to handle multidirectional forces. bi) Stress–strain curve illustrating the elastic and the plastic stages subjected to loads. bii) Comparison of consistent sound absorption in the pristine stage versus deteriorating performance in the deformed stage. c) The expansive air domain within traditional microlattice units, akin to ineffective resonators with inadequate resistance and energy dissipation capabilities. d) Schematic of a general research framework for the interwoven dual-phase design and optimization of microlattice metamaterials.

simultaneously addressing the acoustic disturbances and mechanical stresses. For instance, current metamaterial resonators—such as micro-perforated plates,[6] Fabry–Pérot,[7] and sonic black hole resonators[8]—are effective in sound absorption but are hindered by inferior mechanical properties, exhibiting significant elastic anisotropy and low stiffness. Thus, they are susceptible to deform with irreversible failure under loads.[5a,9]

The emergence of multifunctional materials offers a promising avenue for integrating acoustic and mechanical properties.[10] As a matter of fact, recent studies have investigated innovative approaches, including cellular metamaterials,[11] metasurfaces,[12] and novel research frameworks,[13] to achieve functionality modulation and integration—spanning lightweight design, mechanical rigidity, broadband impedance matching, etc. Recent advancements in multifunctional microlattice metamaterials are poised to revolutionize approaches to sound absorption and mechanical load-bearing challenges.[3c] By leveraging the mechanical advantages inherent in microlattice designs, resonators can be crafted to enhance sound absorption without sacrificing structural integrity. Such multifunctional attributes render them increasingly desirable in contemporary engineering applications. However, achieving the desired elastic response of microlattices remains elusive, as much of the existing research has concentrated on plastic energy absorption. After yielding, pronounced nonlinear stress fluctuations emerge, leading to irreversible large deformations for non-elastic material (Figure 1bi). These deformations significantly deteriorate the resonators within the microlattice, resulting in tearing, fracture, and failure that compromise energy dissipation. Consequently, once irreversible plastic yielding occurs, sound absorption declines precipitously (Figure 1bii). Thus, maintaining the structure in its pristine status is crucial for ensuring consistent sound-absorbing performance.

Moreover, a substantial challenge lies in the intricate structure-multifunctionality relationship within microlattices. The interplay between sound absorption and mechanical properties is closely tied to structural design; specific geometries can profoundly influence how materials respond to both acoustic waves and mechanical stresses. The complexities inherent in their design often hinder optimal performance,[5a,14] with a tendency to focus on enhancing one aspect at the expense of another. Typically, with a reasonable volume fraction, conventional lattice configurations—such as truss and plate lattices—exhibit suboptimal sound absorption,[15] as shown in Figure 1c. Their inherent high porosity creates an expansive air domain through which incident waves can traverse with minimal energy loss, approximating ineffective Helmholtz resonators (HR) characterized by excessively large pores and weak resonance. To address these challenges, existing studies frequently adopt methodologies that compromise mechanical properties. In truss lattices, increasing

 

rod diameter may improve resonance but deteriorate lightweight properties and undermine unit-cell characteristics.[16] Similarly, perforating plates to form micro-perforated panels weakens their stiffness.[17] Although decoupled designs incorporating additional sound absorbers have emerged, they result in highly mechanically anisotropic structures, restricting their use to only applications that can accommodate predictable mechanical deformation resulting from anisotropy.[5b,18] This highlights the need for a universal methodology that overcomes the inherent trade-offs between acoustic and mechanical performance, enabling simultaneous enhancement and optimization of all the desired properties in lattice structures.

In response to these multifaceted challenges, this study introduces a novel additive interwoven dual-phase strategy for the design and optimization of multifunctional microlattice with efficient sound absorption and elastic properties. This approach involves adding a reinforcing phase to the original microlattice phase, aiming to improve sound absorption, local stiffness, and structural integrity. As a proof of concept, a truss microlattice is customized to reinforce an octet truss. This strategy facilitates highly customizable geometric configurations and leverages machine learning alongside multi-objective optimization to enhance multifunctional performance. Experimental results reveal that the optimized microlattices overcome physical limitations, achieving broadband sound absorption, elastic isotropy, and high stiffness. The mechanisms driving these enhancements underscore the effectiveness of this design strategy. This work provides a robust framework for creating acoustically efficient and structurally robust materials.

## 2. Interwoven Strategy and Proof-of-Concept

Efficient elastic properties are crucial for multifunctional materials, ensuring reliable sound absorption (Figure 1bii). Traditional microlattice metamaterials often suffer from low acoustic absorption efficiency (Figure 1c), compounded by the complex geometric relationships that govern multiple functions. The absence of a universal method to maintain geometric symmetry while optimizing these properties poses significant challenges. This work introduces a general research framework for overcoming this challenge (Figure 1d). For a given traditional microlattice, referred to as the original phase (OP), we evaluate whether there are noticeable deficiencies in its essential structural elements, such as rods and shells within the cubic space, as well as the configuration of its air domain. This is achieved by deriving its 1/8-unit crystal structure and analyzing the corresponding air domain. Based on this assessment, we conceptualize a rational reinforcing phase (RP) designed to achieve two primary goals: i) effectively partitioning the expansive air domain to construct the desired resonator architectures (e.g., narrow air channels backed with air cavities), and ii) enhancing load transfer efficiency through increased node connectivity and improved local structural integrity. Generally, the formation of neck-cavity Helmholtz architectures is critical for efficient sound absorption. From a mechanical perspective, it is also essential to assess the spatial configurational complementarity between the OP and RP within the cubic structure. If either objective is not achieved, the design process loops back to re-engineer the RP configuration; once both goals are achieved, an initial artificial design is obtained. Then, optimization can proceed according to the rational interwoven design. Key geometric parameters influencing these functionalities are identified, and predictive models are developed to assess the impact of various geometries on targeted functionalities, utilizing analytical models or machine learning-based networks with datasets sourced from measurements and numerical simulations. Validation criteria ensure the predictive models' accuracy; if these criteria are not met, the models undergo rigorous checks and refinements, supplemented by additional data as necessary. Upon successful validation, multi-objective optimization (MOP) is implemented to optimize competing functional demands, with convergence checks included.

As a proof of concept, the typical octet-truss serves as the original phase, as shown in **Figure** 2a. We begin by investigating its 1/8 crystal structure pattern in a cubic configuration and find that the four struts limit the formation of a dispersed air phase, and desired elastic properties. As such, a reinforcing phase, customized with six struts, is artificially derived based on all these enhancement purposes. As a result, the original air domain is partitioned, evidenced by the formed neck-cavity architecture. Also, the struts distribution becomes rational within the cubic space. The hollow architectures are introduced here for the OP and RP struts to provide lightweight property, and high design freedom in subsequent stiffness modulation. Finally, the dual-phase microlattice is achieved by interweaving the OP and RP. The side length, denoted as $l_0$, is 8 mm in this work. The outer diameter of the struts is designated as $d_{out}$. The inner diameters are denoted as $d_{in}^{OP}$ and $d_{in}^{RP}$ accordingly and $d_{out}$ can also vary for both the OP and RP, which introduces more geometric combinations.

As depicted in Figure 2b, microlattice geometry governs both sound absorption and elastic properties, leading to structural constraints for achieving optimal multifunctionality. Herein, we propose three main indices to characterize the aforementioned functions: i) half-absorption bandwidth ($\Delta B_{0.5}$), a typical measure of absorption performance; ii) normalized Young's modulus $E_n$, which quantifies stiffness under load; and iii) Zener anisotropy index $A$, which assesses elastic anisotropy. Specifically, $d_{out}$ significantly influences sound-absorbing performance by affecting all resonator parameters, including perforation diameter $d_p$, perforation thickness $t_p$, cavity depth $D_e$, and perforation ratio $\sigma_p$ which will be detailed in next section, while let alone the mechanical side as elements. Although $d_{in}^{OP}$ and $d_{in}^{RP}$ affect mechanical properties, they primarily influence the perforation ratio $\sigma_p$ on resonators, as additional tube resonance becomes negligible unless both outer and inner diameters are excessively large.[16,17] As such, in the following sections, we will first analyze the complex geometry-function relationships to gain a deeper understanding of their underlying patterns and mechanisms, followed by constructing mapping models that quantitively capture the geometry-function interactions.

## 3. Results and Discussion

The analytical model for the interwoven dual-phase microlattice is established here. Acoustic impedance under normal incident sound waves is analytically derived. With three repetitive cells in each direction, the resulting 3 × 3 × 3 microlattice has dimensions of 21 mm. This structure can be considered as a

 

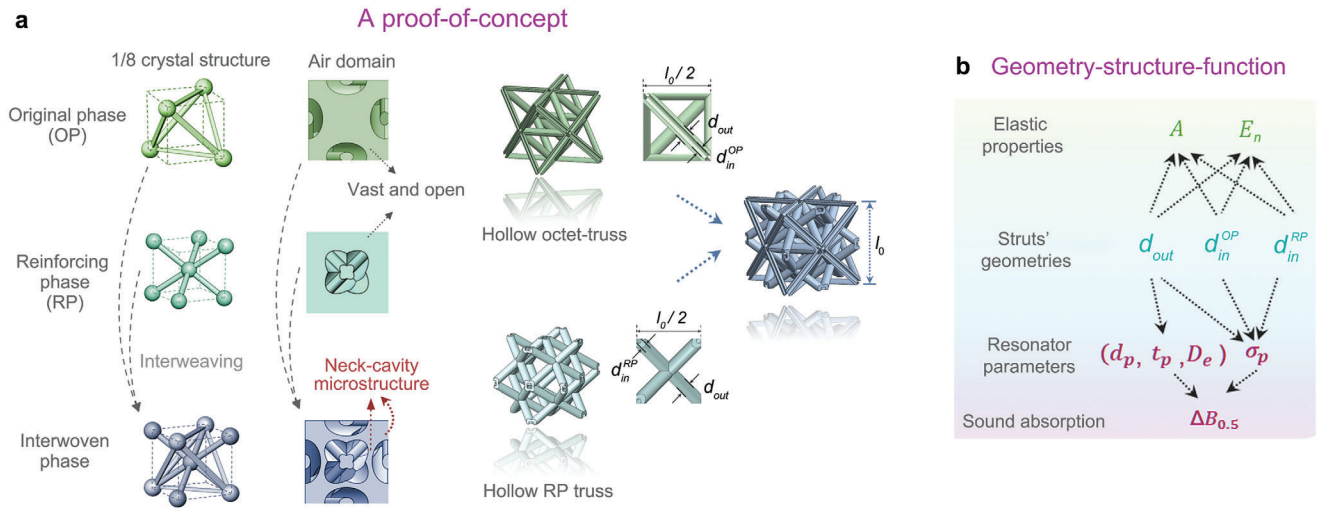


**Figure 2.** Proof-of-concept demonstration and geometry-structure-function relationships. a) A general interweaving design paradigm exemplified by the typical octet-truss, illustrating the selection of a multi-faced reinforcing phase truss derived from crystal configuration analysis, culminating in the final interwoven microlattice. The hollow architecture of the struts provides significant design flexibility for modulating elastic properties. b) Geometry-structure-function relationships, emphasizing the simultaneous influence of geometric parameters on mechanical elasticity and acoustic absorption, thereby highlighting the inherent design constraints of the microlattice.

multi-leveled Helmholtz resonator system, with its acoustic parameters illustrated in **Figure** 3a. The equivalent circuit diagram is plotted based on electro-acoustic theory. $R_l$, $M_l$, and $C_l$ refer to the acoustic resistance, mass, and compliance, respectively, where $l$ refers to the layer number. These items constitute the acoustic impedance for attenuating sounds. As such, the acoustic impedances of micropores $Z_{m,l}$ and cavities $Z_{c,l}$ of the $l$-th layer resonator are calculated. The surface impedance $Z_{s,l}$ is then obtained as

$$Z_{s,l} = Z_{m,l} + Z_{c,l} \tag{1}$$

After calculating the impedance of micro-perforations and cavities (Equations S1–S3, Supporting Information), the sound absorption coefficient ($\alpha$) under an incident sound wave is given as:

$$\alpha = 1 - \left| \frac{Z_s/Z_0 - 1}{Z_s/Z_0 + 1} \right|^2 \tag{2}$$

where $Z_0$ represents the characteristic impedance of air, calculated as $Z_0 = \rho_0 c_0$; $Z_s$ denotes the total surface impedance. The presented analytical model shows a high correlation with the simulated data (Figure S1, Supporting Information) and will be further validated through experimental results in the following sections.

This model only incorporates acoustic parameters, which need to be linked to the geometries of the microlattice. From Figure 3a, $t_p$ remains constant at 0.92 mm, while $D_e$ and $d_p$ are directly determined by $d_{out}$, and the calculation of porosity is detailed in Section S1 (Supporting Information). The dimensions of microlattice indicate that their working frequency region mainly starts from 1.0 kHz. Here, a variable $N_f$ is defined to count the number of points when $\alpha \geq 0.5$ with a frequency step of 1.0 Hz, expressed by Equation (3). This index captures broadband capability of effective absorption, which is suitable for microlattices.[3c] Higher $N_f$ values correspond to enhanced absorption bandwidth.

$$N_f = \Delta B_{0.5} \tag{3}$$

To determine the initial parameters and rational ranges for optimization, the effects of the microlattice strut's inner and outer diameters on sound absorption are elucidated via Figure 3bi,ii, respectively. With $d_{out} = 1.5$ mm held constant, the inner diameters—considered the same for both the OP and RP—generally influence the absorption bandwidth. The first peak shows a slight increase, while a smaller inner diameter is more effective in achieving the wider second peak. In contrast, $d_{out}$ significantly affects absorptive behavior; if it falls below 1.4 mm, a second peak is absent due to the open and vast air domain discussed in Figure 1c. However, an increase in $d_{out}$ will result in higher material density, which will be addressed in subsequent discussions to acquire a balance.

In contrast to acoustic absorption, the hollow level of struts plays a crucial role in microlattice elastic performance. Due to the distinct spatial distributions of the OP and RP, their inner diameters exert different influences on these properties, as illustrated in Figure 3c. Although the outer diameter is kept uniform, numerous geometric combinations would be achieved with varying inner diameters of the OP and RP. Herein, the outer diameter is grouped into 1.25, 1.375, 1.5, and 1.625 mm, while the inner diameters varied from 0.1 to 1.15 mm in steps of 0.075 mm. This comprehensive parameter sweep resulted in a dataset of 900 unique configurations. The representative Volume Element (RVE) approach, combined with periodic boundary conditions (PBCs), is used to compute the elastic properties of microlattice (Section S2, Supporting Information). The Young's modulus $E$ is then calculated and normalized by relative density ($\bar{\rho}$) and material modulus ($E_s$), resulting in the normalized Young's modulus $E_n = E/(\bar{\rho}E_s)$. Extensive simulations are carried out to map the

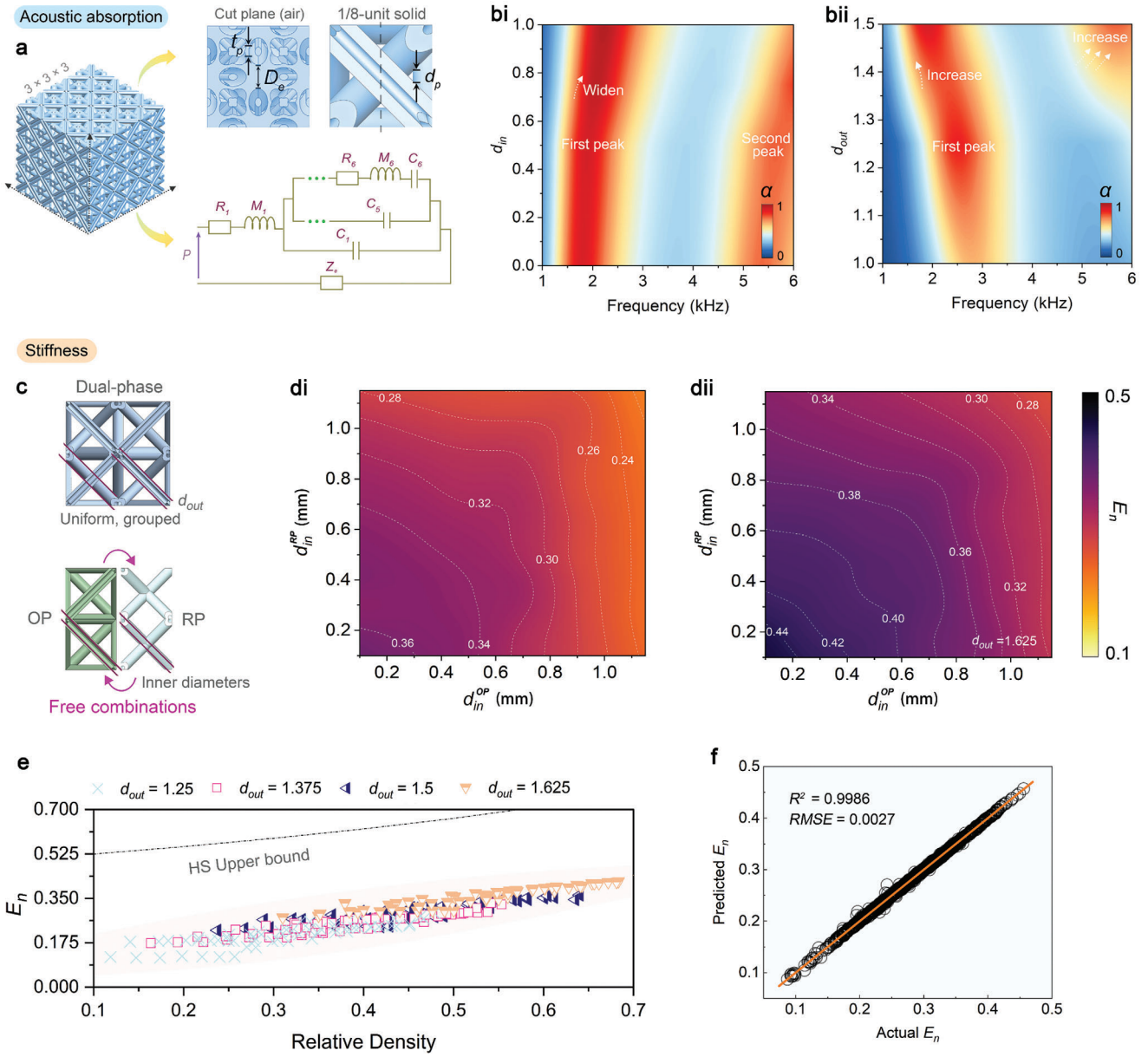


**Figure 3.** Modeling and results. a) Schematic of Helmholtz resonator parameters within a unit cell and the equivalent electro-acoustic circuit for the 3 × 3 × 3 interwoven microlattice. bi, ii) Influence of inner diameters ($d_{out}$ = 1.5 mm) and outer diameter ($d_{in}^{OP} = d_{in}^{RP}$ = 0.5 mm) of struts on sound absorption coefficient. c) Geometric combinations of the interwoven microlattice with fixed outer diameters and varying inner diameters for understanding the geometry-to-stiffness relationships. di, dii) Contour plots of normalized Young's modulus for representative cases (1.5 and 1.625 mm). e) Normalized Young's modulus versus relative density using the representative data points from the simulated dataset. f) High prediction accuracy of the trained ANN model for normalized Young's modulus.

geometric configurations and corresponding elastic properties of the interwoven microlattice. Based on these numerical calculations (see Methods), the geometry-to-stiffness relationships are elucidated before optimization. Two representative cases of $d_{out}$ that contribute to the desired sound absorption behaviors are selected. When it is 1.5 mm (Figure 3di), the inner diameters play a significant role, with smaller diameters leading to higher stiffness due to increased density. With a larger value (Figure 3dii), stiffness increases further, but the influence of the OP and RP are very close, suggesting that huge variations of them are not necessary to achieve the desirable results. To clarify this further, the normalized Young's modulus versus relative density map is given in Figure 3e via representative data points from each group. It shows that while the microlattice achieves a high normalized modulus, it is still below the Hashin–Shtrikman (HS) upper bound. This suggests that although the artificial design is effective, there is a large room for improvement, particularly as high stiffness often contradicts elastic isotropy. For example, ultra-high stiffness could be offered via stiffeners in orthogonal directions but this leads to an extreme anisotropy. For the subsequent

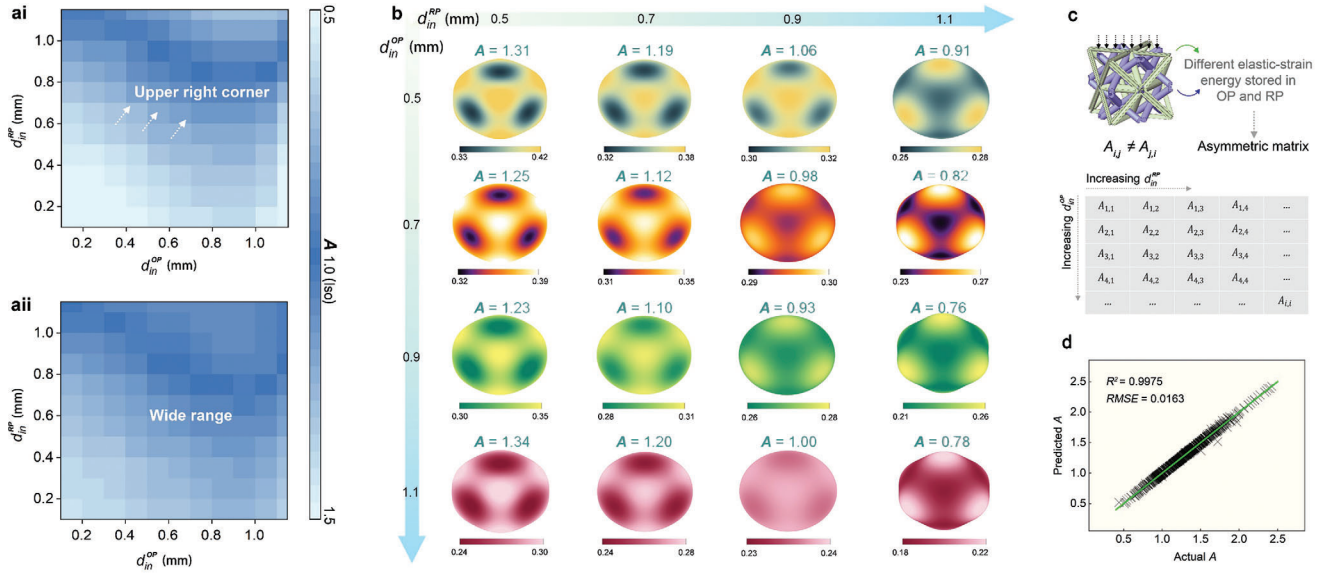


**Figure 4.** Modeling and results. ai, aii) The influence of inner diameters of struts on elastic anisotropy performance of the interwoven microlattice with outer diameters of 1.5 and 1.625 mm shown by heatmap. b) Young's modulus surface of 16 representative cases with varying inner diameters for the OP and RP. c) Different role of the OP and RP in controlling anisotropic performance. d) High prediction accuracy of the trained ANN model for *A*.

optimization, a predictive model correlating inputs ($d_{out}$, $d_{in}^{OP}$, $d_{in}^{RP}$) with outputs $E_n$ is developed. A machine learning approach was utilized to develop an artificial neural network (ANN), leveraging the simulated dataset (see Methods). The model exhibited exceptional predictive accuracy, with an impressive *R*-squared of 0.9986 and a remarkably low Root Mean Squared Error of 0.0027 (Figure 3f).

Elastic properties in any direction can be determined by applying a spatial Euler angle transformation to the compliance matrix (Equation S8, Supporting Information). To quantify elastic anisotropy, the Zener anisotropy index is introduced:

$$A = \frac{2C_{44}}{C_{11} - C_{12}} \tag{4}$$

This index is calculated via the aforementioned RVE methodology. **Figure** 4ai demonstrates how the inner diameters influence the elastic anisotropy. Isotropic elasticity typically occurs in the upper-right region of the map, where $d_{in}^{RP}$ holds a relatively large value, with no strict limitations on $d_{in}^{OP}$. As $d_{out}$ increases, achieving isotropy becomes more feasible, with a broader range of values approaching $A = 1.00$, abbreviated as "Iso" (Figure 4aii). Distinct roles for the OP and RP are observed: when the inner diameter of the RP is small, $A > 1$, indicating greater stiffness along the [111] direction; conversely, when the hollow level of the RP struts increases, $A < 1$, reflecting higher stiffness in axial directions (Figure S3, Supporting Information). After identifying beneficial parameter ranges, we focus on a case with $d_{out} = 1.5$ mm and vary the inner diameters to showcase the versatility of the interwoven design. With the inner diameters ranging from 0.5 to 1.1 mm in 0.2 mm steps, the modulus surface is visualized for 16 configurations (Figure 4b). Even without optimization, most configurations approach elastic isotropy, with one case ($d_{in}^{OP} = 1.1$ mm and $d_{in}^{RP} = 0.9$ mm) achieving total isotropy ($A = 1.00$). In this case, the stiffness distribution resembles a spherical shape, indicating uniform elastic behavior in all loading directions. Moreover, the trend of the inner diameters' influence is complex; there is no simple linear relationship between its changes and the resulting anisotropy performance. Therefore, optimization is essential for fine-tuning anisotropic performance as needed. A distinct asymmetry is observed along the diagonal of Figure 4b, where the results differ significantly on either side. In essence, the difference arises from the varying elastic strain energy stored in the OP and RP under static loads (Figure 4c) owing to their different configuration and node connectivity. Consequently, the anisotropy index $A_{ij} \neq A_{ji}$, where $i$ and $j$ correspond to the inner diameter values of the two substructures. This asymmetry is desirable, as it significantly increases the design freedom for tailoring elastic performance. To characterize how close the actual values are to the ideal isotropic case ($A = 1$), we define a measure $\Delta A$, calculated as $\Delta A = |1 - A|$. The effective range of $A$ is defined as $\Delta A \leq 0.4$, i.e., $A$ ranging from 0.6 to 1.4. The simulated data is used to train a neural network, achieving high accuracy in predicting $A$, as shown in Figure 4d (see details in Section S4, Supporting Information).

The geometry-structure-function relationships are elucidated in previous discussions. Herein, a multi-objective optimization is conducted following the interwoven design, pursuing optimal performance (detailed in Figure 1e). Nondominated sorting genetic algorithm II (NSGA-II) simulating evolution to identify optimal solutions is employed is this work (see Methods). We initially focus on maximizing sound absorption and stiffness with objective functions given in Equation S10 (Supporting Information). The optimal geometries are displayed in **Figure** 5a, showing the $d_{in}^{OP}$ and $d_{in}^{RP}$ are both zero for this problem, i.e., solid struts. This is reasonable since the sound absorption is primarily controlled by $d_{out}$, ranging from 1.52 to 1.60 mm, and the solid struts are essential to secure higher stiffness. The Pareto front is shown

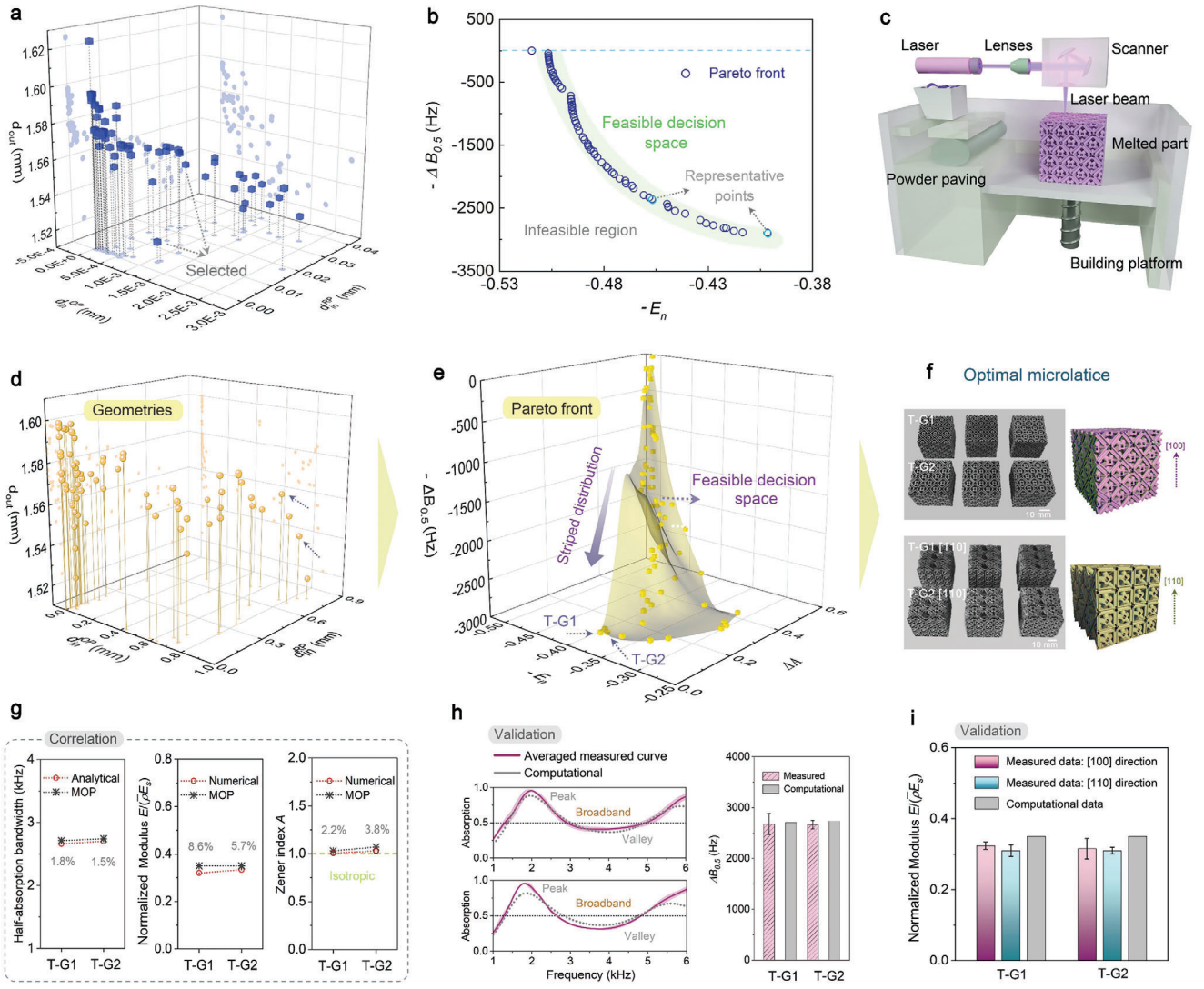


**Figure 5.** Optimization results and validation. Double-objective optimization for broadband absorption and high stiffness: a) optimal microlattice geometries, b) Pareto front map, and c) schematic of the applied SLM technique. Three-objective optimization for broadband absorption, high stiffness, and elastic isotropy: d) optimal microlattice geometries, e) 3D Pareto front map, f) as-printed microlattice samples and virtual models, g) correlation between the predictive and MOP results, and experimental validation for h) sound absorption and i) normalized Young's modulus in both [100] and [110] directions.

in Figure 5b. The computational results demonstrate good convergence, avoiding local optima. Two solutions are selected in the Pareto front, marked as D-G1 and D-G2 with geometries given in Table S2 (Supporting Information). Their $\Delta B_{0.5}$ values are approximately 2.9 and 2.5 kHz, while $E_n$ are 0.4 and 0.44, showing a broadband sound absorption and stiff property. In this study, the microlattices are fabricated via Selective Laser Melting (SLM) with the base material of Ti-6Al-4 V (see Methods). The general procedure for SLM is illustrated in Figure 5c. Sound absorption and quasi-static compression measurements are detailed in the Methods section.

External loads in practical applications may come from various angles (Figure 1a), and thus elastic isotropy, which ensures uniform stiffness across all cubic faces, becomes critical.[4a,19] To address this, we propose a three-objective optimization for optimal all-in-one performance: broadband sound absorption, high stiffness, and elastic isotropy. The objective function is given in Equation S11 (Supporting Information). During early genetic generations of optimization, the distances between individuals remain compact, with minimal variation, and favorable convergence is observed with rapid convergence of the average Pareto distribution, fully stabilizing after around 50 iterations (Figure S4, Supporting Information). Figure 5d displays the 3D distribution of optimal solutions of the input. In the dense region, the struts retain a structure similar to solid rods, as seen in Figure 5a, but there is also a broader, sparse region that accommodates struts with higher hollow levels. Figure 5e illustrates the Pareto solution set, showing a well-distributed, banded appearance. The ideal solution lies in the lower-left corner, but due to strong interdependencies, only relatively optimal solutions are presented. When

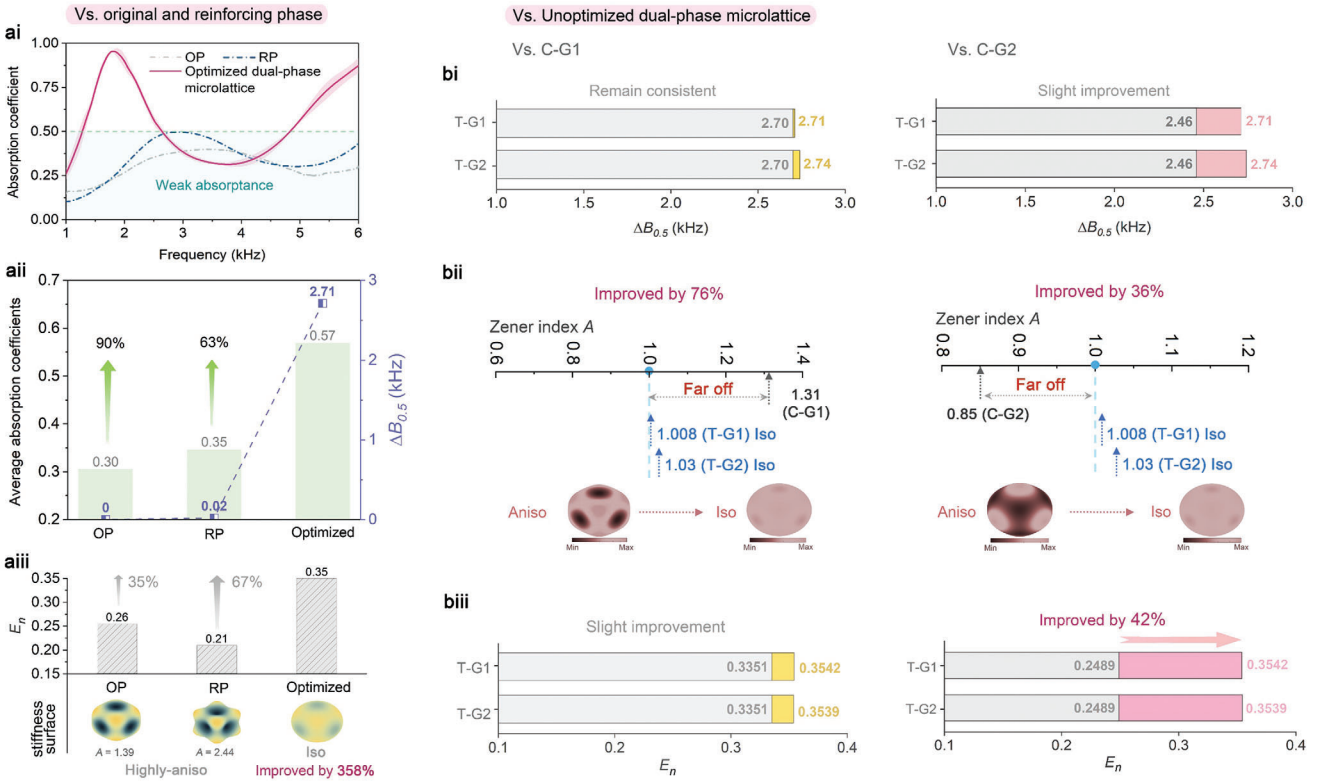


**Figure 6.** Enhancement achieved through the presented interwoven strategy and optimization. Comparison with the original phase and the reinforcing phase sublattices in terms of: ai) sound absorption curves, aii) average absorption coefficients, and aiii) elastic properties. Comparisons with the unoptimized dual-phase microlattices C-G1 and C-G2 in terms of bi) sound absorption curves, bii) elastic anisotropy performance, and biii) normalized Young's modulus.

the absorption bandwidth nears 3000 Hz, $E_n$ positively correlates with $\Delta A$, though most solutions cluster around 2500 Hz. Two parameter sets, designated T-G1 and T-G2, are selected as optimal solutions. Although the inner and outer diameters differ between the two groups, the results are quite similar (Table S3, Supporting Information). The predicted 0.5 absorption bandwidth is around 2.7 kHz, with a normalized modulus of 0.35. Crucially, both groups achieve elastic isotropy, with an $A$ value of 1.008 and 1.03 for T-G1 and T-G2.

The samples and virtual models for the two groups, with three duplicates for each configuration, are displayed in Figure 5f. They are fabricated in both [100] and [110] directions for stiffness measurements (see Section S3, Supporting Information). By inputting the geometries of T-G1 and T-G2 into the predictive models, Figure 5g show the errors for all three metrics—sound absorption (<2%), modulus (6 ~ 9%), and Zener index (<5%)—are minimal, validating the MOP results with no significant deviation observed. Figure 5h presents a comparison between the averaged sound absorption curve from a set of triplicate samples, and the computed curve based on the analytical model, highlighting their respective half-absorption bandwidths. As shown, the measured absorption performance closely matched the computational predictions for both T-G1 and T-G2. Note that the discrepancies in curves stem from 3D printing defects and the applied index, i.e., bandwidth, rather than the full frequency-absorption relationship. Additionally, Figure 5i compares the normalized Young's modulus of the microlattice along [100] and [110] directions, confirming the reliability of the computational model and thereby validating the elastic isotropy shown by modulus surface. The relatively small values in our tests result from the defects of as-printed samples. In brief, the experiments suggest that optimal sound absorption and elastic properties are all achieved in the interwoven microlattice, and the Pareto front provides numerous choices for desired performance.

The optimized microlattices are then compared to unoptimized configurations, including OP, RP, and two unoptimized interwoven microlattices. In **Figure 6**ai, a substantial improvement in sound absorption is observed in the interwoven design compared to the sublattices, transforming their ineffective absorption,[20] i.e., $\alpha < 0.5$, into a broadband high absorption. The resonant frequency shift is attributed to their variations in air domain (Figure S5, Supporting Information). Remarkably, in Figure 6aii, an impressive increase of 90% and 63% in average coefficients is achieved over the OP and RP, respectively. For half-absorption bandwidth, the interwoven microlattice reaches 2.71 kHz, far surpassing the pristine phase structure. This underscores the benefits of the interwoven strategy in facilitating sound absorption. Further improvements in elastic properties are illustrated in Figure 6aiii, where an increase of 35% and 67% in normalized modulus is observed. The interwoven design effectively mitigates the high elastic anisotropy inherent to the sublattices, resulting in a total isotropy. As demonstrated by the surface

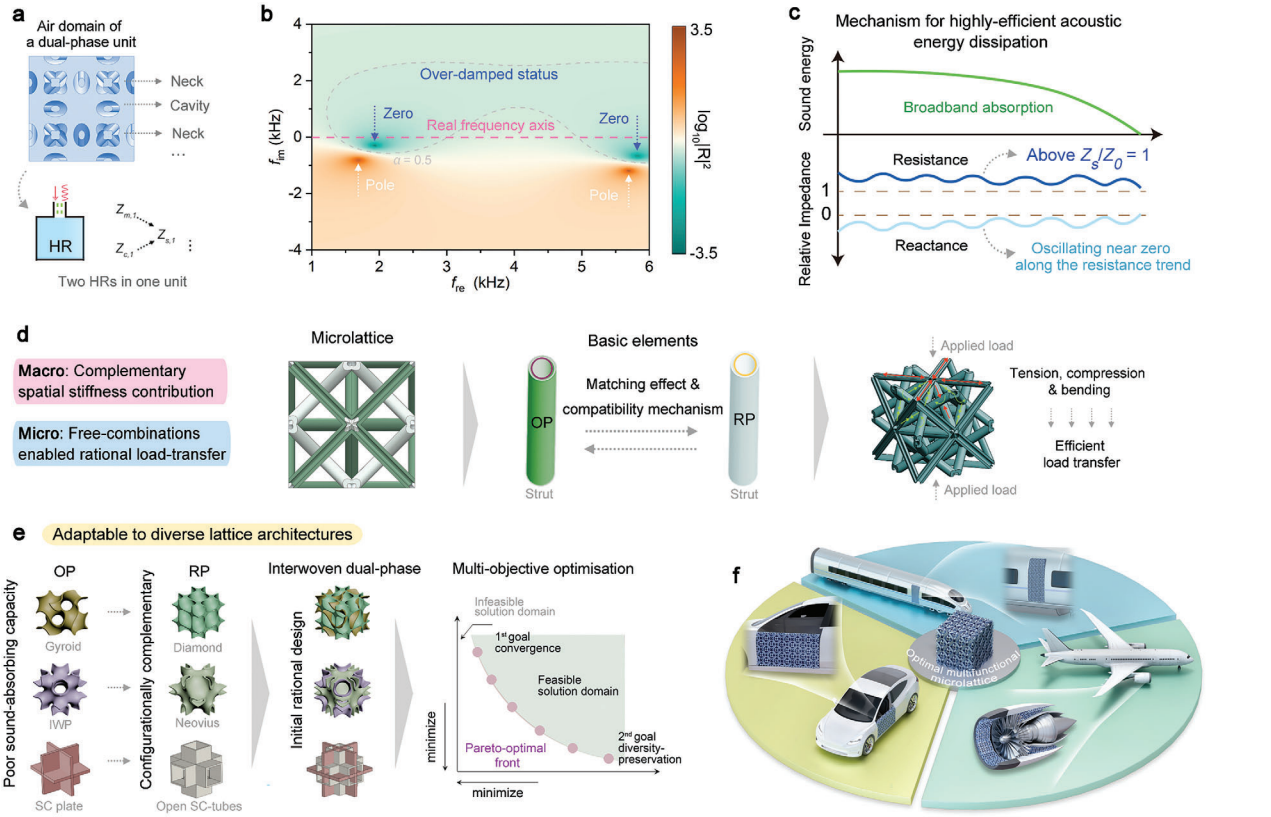


**Figure 7.** Mechanism, flexibility, and application. a) Efficient multi-level cascaded resonant system in one unit cell. b) Representation of the reflection coefficient in the complex frequency plane (T-G1). c) Mechanism for highly-efficient sound energy dissipation. d) Mechanisms for high stiffness and elastic isotropy. e) Illustration of the adaptability of the proposed strategy to various periodic lattice structures, including shell and plate lattice. f) Real word applications of the optimal sound-absorbing and elastically-efficient microlattice.

stiffness distribution, with an aforementioned effective $\Delta A$ of 0.4, the iso-deviation is reduced by up to 358% (Equation S12, Supporting Information).

To further illustrate these gains, two unoptimized dual-phase microlattices, designated C-G1 and C-G2 (Section S5, Supporting Information), which possess varying inner diameters are compared with the optimized microlattice. Within this interwoven design, the sound-absorbing capacity is significantly enhanced, even for these unoptimized cases. The potential for further improvement through MOP appears limited, as evidenced in Figure 6bi, where the increase in $\Delta B_{0.5}$ is modest. However, it is found that the unoptimized microlattice still far from elastic isotropy. Even with RP incorporated to form a spatially rational design, the $A$ values of C-G1 and C-G2 is 1.31 and 0.85, respectively (Figure 6bii). In contrast, our T-G1 case demonstrates an improvement up to 76% and 36% in reducing the iso-derivation. Additionally, a substantial increase in modulus is observed, with a 42% enhancement compared to C-G2 (Figure 6biii).

## 4. Further Discussion

### 4.1. Underlying Mechanisms

The interwoven dual-phase design presented herein integrates diverse functionalities into a single material while offering substantial flexibility for optimization. This approach enables the achievement of optimal performance across multiple properties. The mechanisms responsible for these remarkable enhancements are elucidated in detail below. **Figure** 7a illustrates the air domain of a unit cell within the proof-of-concept microlattice (refer to Figure 2a), designed using the proposed methodology. Within this single unit, distinct necks and cavities are evident, with an additional cavity partitioned into upper and lower sections. This intricate neck-cavity configuration forms a Helmholtz resonator (HR), which is critical for efficient sound absorption. Each HR comprises two elements: the perforation and the cavity. Consequently, the unit can be considered equivalent to two HRs, functioning as a six-layer cascaded resonant system. The reflection coefficient across the complex frequency plane reveals the dissipative features of this structure. As depicted in Figure 7b, the optimized microlattice achieves a slightly over-damped status, with two zeros positioned just below the real frequency axis. This over-damped status is particularly advantageous for a multi-modal system, facilitating the achievement of continuous quasi-perfect broadband absorption.[3c,6,21] Figure 7c illustrates the highly efficient sound absorption mechanism, where incident sound energy is entirely absorbed and dissipated as heat. This process is enabled by optimal impedance matching, characterized by the resistance curve slightly exceeding 1.0 ($Z_s/Z_0 > 1$), indicating a desired resonant condition. Simultaneously, the

reactance curve demonstrates an oscillatory behavior around the zero-axis following the resistance trend. Moreover, introducing parallel coupling of resonant units into the microlattice through a heterogeneous design is crucial for achieving the over-damped resistance shown in Figure 7c. This approach effectively mitigates the pronounced anti-resonance observed around 3 ~ 4 kHz (Figure S7, Supporting Information), thereby enhancing overall sound absorption performance.

In terms of elastic properties, two key mechanisms drive the observed superior performance: i) macroscopic perspective: complementary spatial stiffness distribution; ii) microscopic perspective: rational load transfer enabled by flexible geometric combinations. Using the dual-phase truss structure as an exemplar (Figure 7d), the fundamental building blocks consist of the struts from both the OP and RP phases. These struts possess a hollow architecture, allowing independent variation in outer and inner diameters, resulting in four critical design parameters. This flexibility in geometric combinations generates a vast design space, where specific configurations can lead to enhanced modulus, elastic isotropy, or a finely tuned balance between these properties. Beyond this specific structure, the matching effect between the OP and RP is determined by their respective contributions to stiffness and nodal connectivity. Achieving elastic isotropy depends on configuring them in a complementary manner within 3D space to ensure uniform stiffness distribution. After interweaving, increased nodal connectivity enhances load transfer efficiency, particularly under uniaxial loading conditions. In the octet-truss configuration—focused on herein—tensile and compressive forces dominate. Note that the principles of the presented design can be extended to other configurations, such as shells or plates, which may involve bending or hybrid load cases. In all scenarios, the presented design approach facilitates more effective load transfer, thereby elucidating the exceptional stiffness observed in the optimized microlattices.

### 4.2. Scientific Advance, Flexibility, and Application

The present interwoven strategy opens a new frontier in the design of multifunctional metamaterials, particularly periodic lattice structures that always exhibit weak sound absorption and elastic properties. This approach illustrates how structural symbiosis can unlock superior performance across multiple domains. Distinct from traditional microlattice designs, this strategy simultaneously enhances acoustic absorption and mechanical properties, demonstrates broad applicability to various structural forms (including truss, shell, and plate lattice), and facilitates optimization. The high wide applicability enables the efficient integration of additional functional requirements such as yield strength and energy absorption to be possible.

The versatility of the interwoven design strategy extends well beyond the proof-of-concept explored herein, establishing it as a powerful tool for developing multifunctional metamaterials. This methodology is adaptable to a wide range of periodic lattice structures, including shell lattices such as Triply Periodic Minimal Surfaces (TPMS) and plate lattices, which inherently suffer from poor sound absorption due to their expansive, open-air domains. Some exemplars are provided in Figure 7e. For a given OP, the corresponding RP is identified with aforementioned acoustic and mehcanical considerations (Section 2.1). Once the interwoven design is established, the methodology advances to multi-objective optimization. A Pareto front will be generated, mapping the feasible solution space and providing a diverse range of optimal geometric configurations. This capability not only allows for the fine-tuning of acoustic and elastic properties but also accommodates additional functional requirements—such as plastic deformation, yield strength, or energy absorption—thus opening avenues for more complex demands. With consolidated related criteria, our strategy also works even for complex acoustic-mechanical systems with more demands. Deep learning tools can be used to model complex geometry-structure-function relationships; for instance, the entire frequency-absorption coefficient curve can be used as the output. Similarly, other advanced optimization algorithms tailored to specific challenges are adaptable. From a practical perspective, microlattices can achieve quasi-perfect broadband absorption in the mid-to-high frequency range with simple additions like thin porous layers.[7a] However, achieving desired absorption via lattice structures below 1 kHz demands larger structural dimensions, constrained by the causality principle. For this purpose, our proposed strategy proves pivotal since a sophisticated reinforcing phase to intricately partition the air domain is necessary to dissipate long-wavelength waves. As shown by Figure 7f, potential applications of multifunctional microlattices are broad, spanning transportation, where they can mitigate noise in train and automobile bodies while meeting stringent load-bearing requirements, and aerospace, where they can enhance noise reduction in aircraft engines without compromising mechanical performance as robust acoustic liner. This innovative interwoven strategy provides an efficient pathway for developing high-performance multifunctional materials across various industries.

## 5. Conclusion

This study introduces an interwoven dual-phase strategy for designing a new class of optimal multifunctional microlattice metamaterials that offer superior sound absorption, high stiffness, and isotropic elasticity. As a proof of concept, the conventional octet-truss serves as the original phase, while a reinforcing phase is introduced through spatial topology analysis to create the interwoven design. This strategy facilitates the creation of highly customizable geometric configurations, allowing for the effective integration of machine learning and multi-objective optimization to enhance the multifunctional performance of microlattices. The optimized microlattices demonstrate remarkable enhancements, transforming the sound absorption curve from a sub-0.5 level to a broadband regime above 0.5, increasing stiffness by 67%, and reducing iso-deviation by over 358%. The underlying mechanisms driving these enhancements include the formation of an over-damped resonant system within intricate neck-cavity configurations, facilitating effective sound dissipation and promoting efficient load transfer through a complementary spatial stiffness distribution. By overcoming the structural constraints of traditional microlattice, this strategy is applicable to various structural forms, including truss, shell, and plate configurations. In essence, the interwoven dual-phase strategy not only significantly enhances individual functionality but also demonstrates how structural symbiosis can unlock superior,

optimal performance across multiple domains, paving the way for high-performance solutions that meet the evolving demands of modern engineering challenges.

## 6. Experimental Section

*Finite Element Methods*: Unit-cell models were constructed in ABAQUS to characterize the elastic properties of the presented periodically symmetric microlattices via Python scripting. The script allows free adjustment of geometric parameters. Within ABAQUS's Python environment, it automates the generation of interwoven dual-phase microlattices, meshing, and 1/8-unit cell mirroring with precision and efficiency. The variables are the main geometric parameters of microlattice: $d_{in}^{OP}$, $d_{in}^{RP}$, and $d_{out}$. The RVE homogenization method was adopted for the minimal repetitive unit to facilitate elastic property analysis. PBCs were implemented to provide effective responses by considering the surrounding cells. A 3D lattice model was discretized using C3D10M quadratic tetrahedral elements. Solutions to the partial differential equations defined on a unit cell yielded effective material properties through perturbation theory.

*Computational Prediction and Optimization*: Machine learning technology was employed in this work, utilizing an artificial neural network trained with the bayesian regularization backpropagation algorithm implemented in MATLAB through a multi-layer neural architecture (see Section S3, Supporting Information). NSGA-II was employed for multi-objective optimization, which was configured as follows: the ratio of the Pareto solution set was set to 0.35; with only three variables, the iteration count was 600; the population size was set to 200; the crossover ratio was 0.8; the distance metric function was MATLAB's built-in "distancecrowding"; and the selection method was tournament selection. In each round of the tournament selection method, two or more individuals were randomly chosen from the population, with the one exhibiting the highest fitness score selected. This selection method's advantage lies in its ability to compare only two individuals to determine the superior one, eliminating the need for the actual values of the fitness function.

*3D Printing*: The geometric configurations of microlattices were modeled using SOLIDWORKS software (Dassault Systèmes SOLIDWORKS Corp., USA) and then exported as STereoLithography files for 3D printing. The samples were manufactured using the selective laser melting via XDM 250 machine (XDM 3D printing Co., Ltd., China) technique with Ti6Al4 V as the material of choice. The laser system employed was a 500 W Yb fiber laser (IPG) with a beam diameter of 80 µm. The optical setup included an F-theta lens paired with a high-speed, high-precision scanner. The disk laser operated at 500 W, with a printing layer thickness of 20 µm. After printing, the specimens were wire-cut from the substrate and subjected to post-processing steps, including residual powder removal, stress-relieving treatment, ultrasonic cleaning, and drying in a blow-dryer oven. The material parameters were determined through tensile tests conducted on an Instron 8501 apparatus. The material parameters included Young's modulus $E_s$ of 104 GPa, initial yield strength $\sigma_0$ of 864 MPa, Poisson's ratio $\upsilon$ of 0.3, and density $\rho_s$ of 4.43 g/cm$^3$.

*Measurements*: A standard two-microphone setup was utilized for sound absorption coefficient measurements following ISO 10534-2 standards (ZT13, SKC Acoustics Technology Co., Ltd., China). The samples were cut from the cubic model to fit into a cylindrical holder with a diameter of 30 mm. For better printing precision, they were divided into two halves and fabricated separately. During testing, the halves were combined and wrapped together. All reported absorption coefficients were averaged from three datasets. Compression experiments were conducted using an Instron 1346 universal testing machine. The samples were subjected to axial quasi-static loading at a strain rate of 0.001 s$^{-1}$. Compression was directed along the parallel pair of faces aligned with the SLM building direction. The materials were centrally positioned on the plate and compressed unidirectionally by a mobile rigid plate until densification was achieved. For accurate measurement of Young's modulus, strain compensation was performed for the testing apparatus itself. The experimental findings were systematically presented as three sets of averaged results supplemented by their corresponding standard deviations.

## Supporting Information

Supporting Information is available from the Wiley Online Library or from the author.

## Acknowledgements

The authors would like to thank Michael Zaiser for the fruitful discussions. This research was supported by NSFC/RGC Joint Research Scheme sponsored by the Research Grants Council of Hong Kong and the National Natural Science Foundation of China (N_PolyU553/23), RGC Theme-based Research Scheme (P0053908 under parent project P0047801), National Key R&D Program of China (2022YFB4300101), Hunan Provincial Natural Science Foundation of China (2023JJ10074), and Science and Technology Innovation Program of Hunan Province (2023RC1011).

## Conflict of Interest

The authors declare no conflict of interest.

## Data Availability Statement

The data that support the findings of this study are available from the corresponding author upon reasonable request.

## Keywords

3D printing, mechanical metamaterial, microlattice, sound absorption, structure design

Received: October 23, 2024
Revised: November 22, 2024
Published online:

[1] S. A. Stansfeld, B. Berglund, C. Clark, I. Lopez-Barrio, P. Fischer, E. Öhrström, M. M. Haines, J. Head, S. Hygge, I. Van Kamp, *Lancet* **2005**, *365*, 1942.
[2] M. Basner, W. Babisch, A. Davis, M. Brink, C. Clark, S. Janssen, S. Stansfeld, *Lancet* **2014**, *383*, 1325.
[3] a) S. Huang, Y. Li, J. Zhu, D. P. Tsai, *Phys. Rev. Appl.* **2023**, *20*, 010501; b) Z. Li, W. Zhai, X. Li, X. Yu, Z. Guo, Z. Wang, *Virtual Phys. Prototyping* **2022**; c) X. Li, J. W. Chua, X. Yu, Z. Li, M. Zhao, Z. Wang, W. Zhai, *Adv. Sci.* **2024**, *11*, 2305232.
[4] a) Y. Wang, F. Xu, H. Gao, X. Li, *Small* **2023**, *19*, 2206024; b) F. Wang, O. Sigmund, *J. Mech. Phys. Solids* **2021**, *152*, 104415.
[5] a) Z. Li, X. Wang, K. Zeng, Z. Guo, C. Li, X. Yu, S. Ramakrishna, Z. Wang, Y. Lu, *NPG Asia Mater.* **2024**, *16*, 45; b) Z. Li, X. Li, Z. Wang, W. Zhai, *Mater. Horiz.* **2023**, *10*, 75.
[6] Z. Zhou, S. Huang, D. Li, J. Zhu, Y. Li, *Natl. Sci. Rev.* **2022**, *9*, nwab171.
[7] a) M. Yang, S. Chen, C. Fu, P. Sheng, *Mater. Horiz.* **2017**, *4*, 673; b) Y. Zhu, A. Merkel, K. Donda, S. Fan, L. Cao, B. Assouar, *Phys. Rev. B* **2021**, *103*, 064102.
[8] G. Serra, O. Guasch, M. Arnela, D. Miralles, *Mech. Syst. Signal Proc.* **2023**, *202*, 110707.
[9] a) Y. Tang, F. Li, F. Xin, T. J. Lu, *Mater. Des.* **2017**, *134*, 502; b) Z. Wang, Z. Guo, Z. Li, K. Zeng, *Virtual Phys. Prototyping* **2023**, *18*, e2111585; c) X. Li, M. Zhao, X. Yu, J. W. Chua, Y. Yang, K. M. Lim, W. Zhai, *Mater. Des.* **2023**, *234*, 112354; d) Y. Liu, B. Xia, K. Liu, Y. Zhou, K. Wei, *J. Mech. Phys. Solids* **2024**, *190*, 105751.

[10] Z. Zhu, D. W. H. Ng, H. S. Park, M. C. McAlpine, *Nat. Rev. Mater.* **2021**, *6*, 27.
[11] D.-G. Zhao, Y. Li, X.-F. Zhu, *Sci. Rep.* **2015**, *5*, 9376.
[12] Z.-L. Li, K. Chen, F. Li, Z.-J. Shi, Q.-L. Sun, P.-Q. Li, Y.-G. Peng, L.-X. Huang, G. Yang, H. Zheng, *Nat. Commun.* **2023**, *14*, 5319.
[13] X. Yang, Z. Zhang, M. Xu, S. Li, Y. Zhang, X.-F. Zhu, X. Ouyang, A. Alù, *Nat. Commun.* **2024**, *15*, 4346.
[14] X. An, C. Lai, W. He, H. Fan, *Composites, Part B* **2021**, *224*, 109232.
[15] a) T. G. Zieliński, K. C. Opiela, P. Pawłowski, N. Dauchez, T. Boutin, J. Kennedy, D. Trimble, H. Rice, B. Van Damme, G. Hannema, *Addit. Manuf.* **2020**, *36*, 101564; b) K. C. Opiela, T. G. Zieliński, *Composites, Part B* **2020**, *187*, 107833; c) W. Yang, J. An, C. K. Chua, K. Zhou, *Virtual Phys. Prototyping* **2020**, *15*, 242.
[16] X. Li, X. Yu, W. Zhai, *Small* **2022**, *18*, 2204145.
[17] Z. Li, X. Wang, X. Li, Z. Wang, W. Zhai, *ACS Appl. Mater. Interfaces* **2023**, *15*, 9940.
[18] J. W. Chua, X. Li, X. Yu, W. Zhai, *Compos. Struct.* **2023**, *304*, 116434.
[19] C. Bonatti, D. Mohr, *J. Mech. Phys. Solids* **2019**, *122*, 1.
[20] Z. Li, X. Li, X. Wang, Z. Wang, W. Zhai, *ACS Appl. Mater. Interfaces* **2023**, *15*, 24868.
[21] M. Yang, P. Sheng, *Appl. Phys. Lett.* **2023**, 122.